JGR Solid Earth

RESEARCH ARTICLE
10.1029/2019JB019256

# Constraints on the Depth, Thickness, and Strength of the G Discontinuity in the Central Pacific From S Receiver Functions

**H. F. Mark[1], J. A. Collins[2], D. Lizarralde[2], G. Hirth[3], J. B. Gaherty[4], R. L. Evans[2], and M. D. Behn[5]**

[1]Department of Earth and Planetary Sciences, Washington University in St. Louis, St. Louis, MO, USA, [2]Department of Geology and Geophysics, Woods Hole Oceanographic Institution, Woods Hole, MA, USA, [3]Geological Sciences Department, Brown University, Providence, RI, USA, [4]School of Earth and Sustainability, Northern Arizona University, Flagstaff, Arizona, USA, [5]Department of Earth and Environmental Sciences, Boston College, Chestnut Hill, MA, USA

**Key Points:**

- We image a seismic discontinuity centered at 65 km depth in the central Pacific upper mantle
- Co-located constraints on seismic velocities, anisotropy, and attenuation also show transitional features at 60–80 km depth
- The observed discontinuity may represent a zone of localized shear within a broader zone accommodating relative plate motion

**Supporting Information:**

- Supporting Information S1
- Table S1
- Table S2

**Correspondence to:**
H. F. Mark,
hmark@wustl.edu

**Citation:**
Mark, H. F., Collins, J. A., Lizarralde, D., Hirth, G., Gaherty, J. B., Evans, R. L., & Behn, M. D. (2021). Constraints on the depth, thickness, and strength of the G discontinuity in the central Pacific from S receiver functions. *Journal of Geophysical Research: Solid Earth*, *126*, e2019JB019256. https://doi.org/10.1029/2019JB019256

Received 16 DEC 2019
Accepted 3 MAR 2021



**Abstract** The relative motion of the lithosphere with respect to the asthenosphere implies the existence of a boundary zone that accommodates shear between the rigid plates and flowing mantle. This shear zone is typically referred to as the lithosphere-asthenosphere boundary (LAB). The width of this zone and the mechanisms accommodating shear across it have important implications for coupling between mantle convection and surface plate motion. Seismic observations have provided evidence for several physical mechanisms that might help enable relative plate motion, but how these mechanisms each contribute to the overall accommodation of shear remains unclear. Here we present receiver function constraints on the discontinuity structure of the oceanic upper mantle at the NoMelt site in the central Pacific, where local constraints on shear velocity, anisotropy, conductivity, and attenuation down to ~300 km depth provide a comprehensive picture of upper mantle structure. We image a seismic discontinuity with a Vsv decrease of 4.5% or more over a 0–20 km thick gradient layer centered at a depth of ~65 km. We associate this feature with the Gutenberg discontinuity (G), and interpret our observation of G as resulting from strain localization across a dehydration boundary based on the good agreement between the discontinuity depth and that of the dry solidus. Transitions in Vsv, azimuthal anisotropy, conductivity, and attenuation observed at roughly similar depths suggest that the G discontinuity represents a region of localized strain within a broader zone accommodating shear between the lithosphere and asthenosphere.

## 1. Introduction

Observations of surface plate motions and changes in seismic anisotropy in the upper mantle indicate that the lithosphere moves relative to the underlying asthenospheric mantle (e.g., Becker, 2008; Conrad et al., 2007; Savage, 1999; Solomon & Sleep, 1974; Wilson, 1965). This implies the existence of a transition where the shear strain between the rigid plate and flowing mantle is accommodated over some depth range. The transition is often referred to as the lithosphere-asthenosphere boundary (LAB), but whether it is actually a sharp, boundary-like feature or is instead a broader, more diffuse zone of deformation is not well understood (e.g., Fischer et al., 2010). The sharpness of the transition and the physical changes occurring across it have implications for coupling between the plates and the convecting mantle and, as a result, for the wavelength of mantle convection and the balance of forces that drive plate tectonics (e.g., Ghosh et al., 2008; Höink et al., 2011; Lenardic et al., 2006; Richards & Lenardic, 2018; Richards et al., 2001).

Several physical mechanisms have been proposed to explain the rheological transition from the lithosphere to the asthenosphere, but no single factor is able to explain all the relevant observations of the upper mantle. The primary factors thought to contribute to the rheological contrast are temperature, composition, and melt. Temperature strongly influences viscosity, and seismic tomography models of the oceanic upper mantle show a broad gradient from fast seismic velocities in the shallow mantle to slower velocities in the asthenosphere that is thought to represent the effects of plate cooling (e.g., Beghein et al., 2014; Maggi et al., 2006). However, the temperature dependence of rock properties cannot explain all seismic observations of the lithosphere (Faul & Jackson, 2005; Jackson et al., 2002; Stixrude & Lithgow-Bertelloni, 2005). In particular, thermal gradients are not sharp enough to produce the abrupt changes in seismic velocities, or

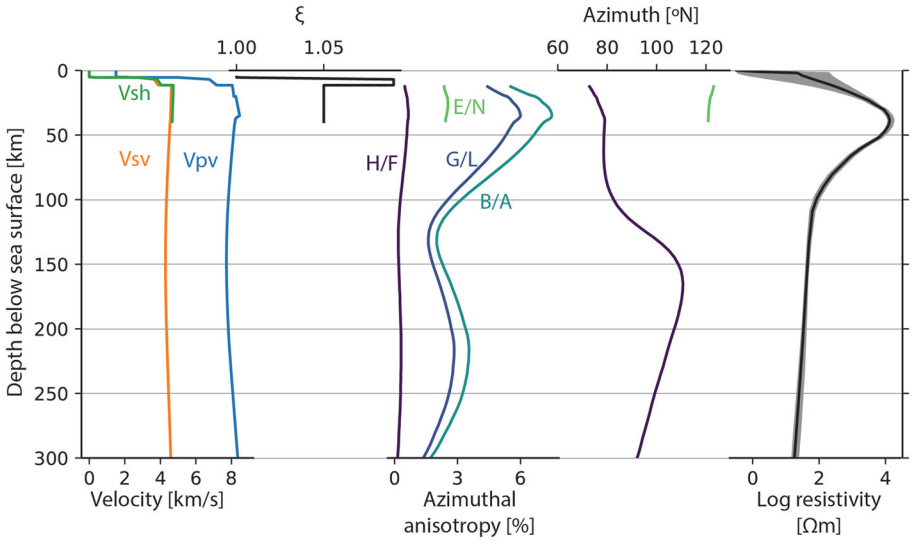


**Figure 1.** Local constraints on seismic and electrical structure from previous studies using NoMelt data, including seismic velocities, radial anisotropy, and the strength and orientation of azimuthal anisotropy from Lin et al. (2016) and Russell et al. (2019); and electrical resistivity from Sarafian et al. (2015). The anisotropy parameters A, L, N, and F are Love's parameters (Montagner & Nataf, 1986), which can be used to describe azimuthally averaged radial anisotropy. The parameters B, G, E, and H describe the azimuthal variation of A, L, N, and F, respectively. Together, these eight parameters are sufficient to describe the complete elastic tensor for a weakly anisotropic solid.

seismic discontinuities, observed in the upper mantle (e.g., Fischer et al., 2010; Rychert & Harmon, 2018). Mantle composition also influences viscosity, and compositional gradients are expected within the upper mantle due to melting and melt extraction at mid-ocean ridges (Braun et al., 2000; Hirth & Kohlstedt, 1996; Phipps Morgan, 1997). Strong gradients in mantle water content resulting from ridge processes could explain observations of seismic discontinuities at roughly constant depths in the oceanic upper mantle. Discontinuities have been observed at 50–100 km depth beneath the oceans, and are often referred to as the Gutenberg, or G, discontinuity (Gutenberg, 1959; Revenaugh & Jordan, 1991). However, discontinuity observations in the oceanic upper mantle are spatially heterogeneous and some studies have found that the depth of G varies with plate age (e.g., Kumar & Kawakatsu, 2011; Rychert & Shearer, 2011; Schmerr, 2012). Such an age-dependence would be inconsistent with models that invoke compositional gradients established during plate formation to explain observations of G. The presence of melt can reduce mantle viscosity, and horizontal melt-rich layers at the base of the lithosphere could facilitate plate motion and explain discontinuity observations, in particular observations of discontinuities that deepen with increasing plate age (Hammond & Humphreys, 2000; Kawakatsu et al., 2009; Rychert et al., 2018; Schmerr, 2012). However, in the absence of other tectonic complications such as petit-spot volcanism near subduction zones (e.g., Hirano, 2011; Yang & Faccenda, 2020), melt is not expected to be stable beneath old, cold oceanic lithosphere far from the ridge axis although seismic discontinuities are still observed in these regions.

The NoMelt experiment offers an exceptional opportunity to address questions related to the structure of the oceanic upper mantle and the nature of the lithosphere-asthenosphere transition by providing multiple types of high-resolution geophysical data at a single location. The experiment deployed an array of ocean bottom seismometers (OBS) and magnetotelluric (MT) instruments in the center of a stable spreading segment in the Pacific where the plate is ~70 Myr old and appears to have a simple tectonic history. Data from NoMelt have been used to constrain local shear velocity, seismic anisotropy, attenuation, and electrical conductivity through the shallow upper mantle (Lin et al., 2016; Ma et al., 2020; Mark et al., 2019; Matsuno & Evans, 2017; Russell et al., 2019; Sarafian et al., 2015) (Figure 1). These smooth models for local Vs and azimuthal anisotropy at the NoMelt site agree well with regional tomographic models (e.g., Gaherty et al., 1996).

This study uses OBS receiver functions to constrain the upper mantle discontinuity structure at the NoMelt site. The receiver functions indicate that a discontinuity is present beneath the NoMelt array as a velocity

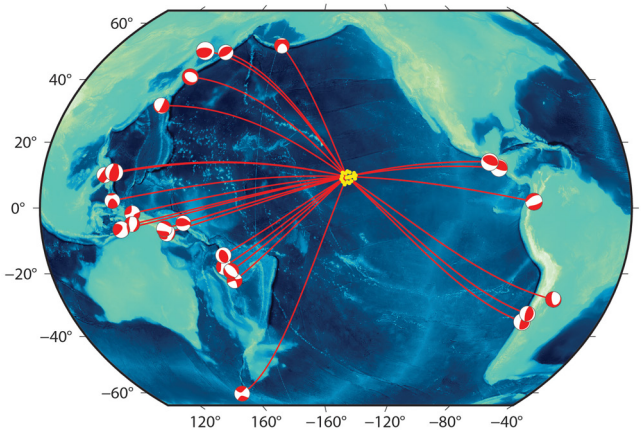


**Figure 2.** Map of the Pacific showing the location of the NoMelt broadband OBS array (yellow dots), and the locations and focal mechanisms of the 25 events used in this study (beachballs). See Table S1 for a list of all event-station pairs used.

decrease of 4.5% or more with a thickness of 0–20 km and a mean depth of ~65 km. The observed discontinuity, which we associate with the G discontinuity, is interpreted as a region of localized strain associated with dehydration. Overall, observations from NoMelt suggest that the discontinuity is part of a broader shear zone that accommodates the relative motion of the lithosphere with respect to the asthenosphere.

## 2. Data and Methods

We calculate and analyze receiver functions from broadband OBS data collected as part of the NoMelt experiment with the aim of identifying seismic discontinuities in the shallow oceanic upper mantle and quantifying the discontinuous seismic structure in sufficient detail to place constraints on the physical mechanism(s) that give rise to this structure. After selecting relevant earthquake data and applying quality controls, receiver functions are calculated using the extended-time multitaper method (Helffrich, 2006; Park & Levin, 2000; Park et al., 1987; Shibutani et al., 2008). The receiver functions are corrected for moveout using velocity models based on local models for the NoMelt site (Lin et al., 2016; Lizarralde et al., 2018; Russell et al., 2019) and the PA5 model for a corridor in the western Pacific (Gaherty et al., 1996). The moveout-corrected traces are then stacked to enhance signals from converted phases. Synthetic receiver functions are calculated in the same manner from reflectivity synthetic seismograms using a set of velocity models spanning a parameter space where the depth, thickness, and strength of an upper mantle seismic discontinuity are varied. Finally, two quantitative parameters are extracted from each receiver function stack: the time and the normalized amplitude of the receiver function peak attributed to the converted *Sp* phase from a shallow upper mantle discontinuity. The parameters extracted from the receiver function stacks for the data are compared to predictions from the synthetic receiver function stacks, and the comparisons are used to assess which models for the discontinuity structure beneath the NoMelt array are able to explain the observations.

### 2.1. Geophysical Context from NoMelt

The NoMelt experiment aimed to characterize the detailed seismic and electrical structure of the oceanic lithosphere-asthenosphere system in the central Pacific at a location where the plate does not appear to have experienced any substantial tectonic or magmatic disturbance since its formation (Figure 2). The experiment was conducted in the middle of a stable spreading segment between the Clarion and Clipperton fracture zones, where the plate is ~70 Myr old (Barckhausen et al., 2013). The experiment consisted of a ~1 year deployment of 26 broadband OBS and eight MT instruments, along with the acquisition of active-source seismic refraction and reflection data using 31 short-period OBS and a 6 km long multi-channel streamer.

Data from NoMelt constrain the smooth seismic and electrical structure of the mantle down to ~300 km depth beneath the sea surface. Surface waves have been used to infer local *S* velocity structure through the asthenosphere (Figures 1a–1d) (Lin et al., 2016; Russell et al., 2019). The overall structure resembles regional models (e.g., Gaherty et al., 1996; Tan & Helmberger, 2007), with a high-velocity lid overlying a low-velocity zone (LVZ). Changes in the strength and orientation of azimuthal anisotropy with depth suggest that shallow mineral fabric is locked into the lithosphere during plate spreading while deeper fabric in the asthenosphere is modified by subsequent mantle flow, likely a combination of pressure gradient-driven return flow and secondary convection (Lin et al., 2016). Models for the electrical structure at the NoMelt site based on MT data show a resistive lid ~60–80 km thick overlying more conductive mantle (Figure 1e) (Matsuno & Evans, 2017; Sarafian et al., 2015). This can be explained by a change in water content from a dry lid to an underlying region with greater hydrogen saturation within nominally anhydrous olivine, and is inconsistent with the presence of interconnected melt beneath the lid (Matsuno & Evans, 2017; Sarafian et al., 2015). The attenuation structure derived from long-period Rayleigh waves crossing the NoMelt array can be modeled using two layers, with a transition from low attenuation ($Q$ = 1,400) above 60 km depth to high attenuation ($Q$ = 110) below 80 km (Ma et al., 2020).

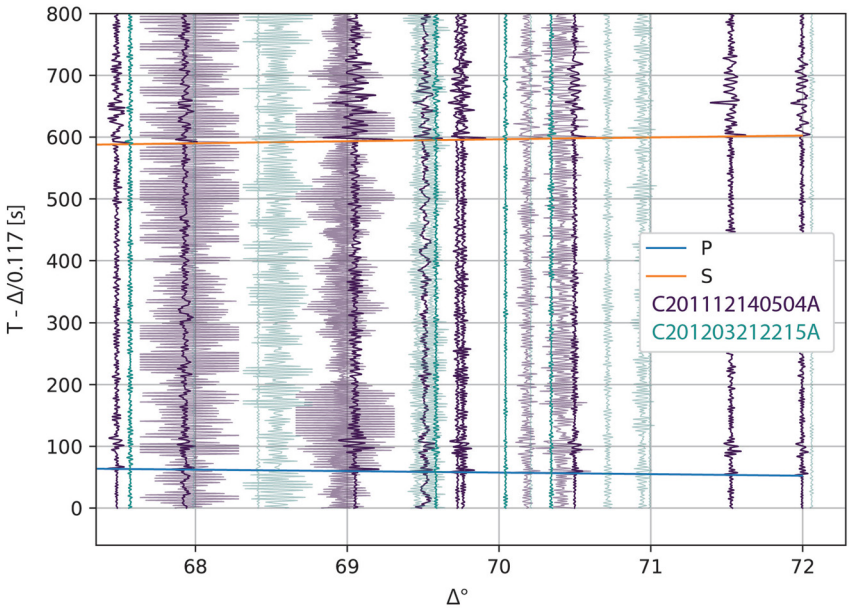


**Figure 3.** A record section showing radial component data from two events at similar distances from the NoMelt array, with direct phase arrival times predicted for the global velocity model *ak135* shown by the blue (*P*) and orange (*S*) horizontal lines (Kennett et al., 1995). The data are filtered to 4–35 s. Traces are color-coded by event. Dark lines correspond to traces used in this study, while lighter lines are traces discarded during quality control due to either lack of a distinct direct *S* phase or low SNR. Both events originated near New Guinea. See Table S1 for a full list of event-station pairs used in this study.

### 2.2. Data Selection and Processing

During the NoMelt broadband OBS deployment, 28 circum-Pacific earthquakes occurred that meet our initial selection criteria of $M_W \geq 6.5$ and source-to-station ranges between 50° and 90° (Figure 2). The 50°–90° range is suitable for *S*-to-*p* receiver functions targeting shallow upper mantle structure (Yuan et al., 2006). Terrestrial receiver function studies are often able to use events with magnitudes lower than $M_W$ 6.5 (e.g., Hopper et al., 2014), but larger events are needed for OBS studies to overcome microseismic and current noise in the submarine environment. While a high magnitude threshold severely limits the amount of usable data, the signal-to-noise ratio for records of smaller events is too low in the frequency band used for the receiver function calculation (0.0286–0.25 Hz).

The data are initially processed by performing a component rotation, filtering, and controlling for data quality. The horizontal components of the seismograms are rotated to radial and transverse orientations, and the data are then bandpass filtered to 4–35 s (0.0286–0.25 Hz). This passband is chosen to exclude most long-period noise from infragravity waves, tilt, and compliance, and to attenuate short-period microseismic noise, while retaining earthquake energy over a broad enough band for the receiver function deconvolution process to work. Tests including slightly higher frequencies resulted in significantly noisier data. The direct *S* phase is then picked on the radial component using the Z detection algorithm (Swindell & Snell, 1977; Withers et al., 1998). Traces where *S* is not detected within 20 s of the arrival time predicted by the global velocity model *ak135* are excluded from subsequent analyses. All traces and picks are also visually inspected to ensure that the algorithm is neither excluding usable data nor giving erroneous picks. Finally, traces with a signal-to-noise ratio (SNR) less than 1.2 on the radial component are excluded (Figure 3). The SNR is calculated as the ratio of the maximum amplitude between 5 s before and 50 s after the picked time for direct *S* to the maximum amplitude in a 120-s window ending 30 s before the predicted arrival time of direct *P*. The choice of the SNR threshold is based on tests with synthetic seismograms (see Figure S2), and is intended to balance the need for strong signals with the limited amount of data available. After quality control, we retain data for 125 station-event pairs from 25 events and 15 stations (Table S1).

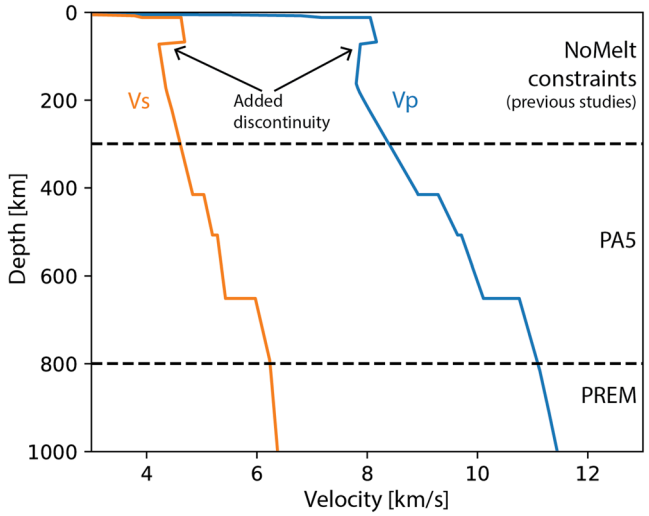


**Figure 4.** The seismic velocity model used to calculate the synthetics in Figure 5d. 0 km corresponds to the sea surface. The upper 300 km of the model are modified from the models of Lin et al. (2016), Lizarralde et al. (2018), and Russell et al. (2019), with the addition of a discontinuity as a gradient at 70 ± 2.5 km depth where Vsv drops by 10.5%. Between 300 and 800 km, the model is modified from PA5 (Gaherty et al., 1996). From 800 km down to the outer core boundary, the model follows PREM (Dziewonski & Anderson, 1981). The model is truncated at the outer core boundary.

### 2.3. Receiver Function Calculation

We calculate *S* receiver functions using the extended-time multitaper method (Helffrich, 2006; Park & Levin, 2000; Park et al., 1987; Shibutani et al., 2008) to look for converted *Sp* phases from shallow mantle discontinuities (e.g., Kawakatsu et al., 2009; Kumar et al., 2005). *S* receiver functions are well-suited to imaging shallow discontinuities, because converted phases from these features arrive fairly close in time to their parent phases. Thus, a converted *Sp* arriving before direct *S* is less likely to be obscured by multiples and coda than *Ps* from a shallow discontinuity. The extended-time multitaper method entails windowing the time-series data with a set of Slepian tapers before transformation to the frequency domain to obtain noise-resistant spectral estimates (Helffrich, 2006; Park et al., 1987). We use 3 prolate eigentapers, a time-bandwidth product of 4, a taper length of 10 s, and 75% window overlap for the receiver function calculation (Helffrich, 2006; Shibutani et al., 2008). Before applying the tapers, the data are rotated from ZRT into LQT coordinates to separate upgoing *Sv* (Q) from *P* (L). The LQT rotation angle is calculated by ray-tracing through a one-dimensional (1D) model representative of the NoMelt site (see Section 2.4). The presence of a thin sediment layer results in near-vertical upgoing rays, so the angle is quite small (~5°). Therefore, while LQT rotation is typically included in receiver function processing, in this and similar cases its effects are likely to be negligible. The Q component is trimmed to 10 s before and 30 s after the direct *S* arrival, and the L component is trimmed to 50 s before and 30 s after.

The receiver functions are stacked to increase the signal-to-noise ratio. The quantity of data is not sufficient to stack traces for individual stations or sections of the OBS array (see Section 2.4), so we stack all of the traces together. A moveout correction is applied to the receiver functions before stacking to correct for the fact that converted phase arrival times depend on range. The moveout correction is referenced to a range of 70°, and it is calculated using a velocity model with a set discontinuity structure. The choice of the moveout velocity model is discussed in Section 2.6. Stacks are calculated as an unweighted mean of all moveout-corrected traces. Stack uncertainty is estimated using bootstrap stacking. Bootstrap samples of 125 traces are drawn randomly with replacement from the set of 125 individual receiver functions. This sampling process is repeated 300 times to generate an ensemble of stacks which are then used to calculate the standard deviation of the receiver function amplitude for each point in the time series.

Receiver function amplitudes are normalized to the amplitude of the peak associated with the Moho conversion, approximately 1 s before direct S. This peak in the receiver functions primarily represents an *S*-to-*p* conversion at the Moho, but also includes some contributions from a conversion at the crust-sediment interface. The maximum amplitude of the Moho peak in the stack of all moveout-corrected traces is used as the normalization factor for the overall stack and for each of the bootstrap stacks.

### 2.4. Synthetic Sensitivity Tests

Synthetic tests demonstrate that inferences about upper mantle discontinuities can be made based on stacks with a sufficiently large number of traces (~100 or more). Reflectivity synthetic seismograms are calculated (e.g., Kennett & Kerry, 1979) using the event moment tensors, source-station back azimuths, and ranges from the NoMelt data set. The synthetic seismograms are calculated for velocity models which include a shallow upper mantle discontinuity that we will refer to as G. The depth, thickness, and velocity drop across the discontinuity are varied between the different velocity models, with one example shown in Figure 4. The models include both sediments and water, and reverberations in these layers are accounted for in the reflectivity calculation. The water depth and sediment thickness are taken to be the average values across the NoMelt site, based on high-resolution bathymetry and seismic reflection data. This results in 5,220 m of water and 165 m of sediment, and the synthetics are calculated for stations located at the water-sediment

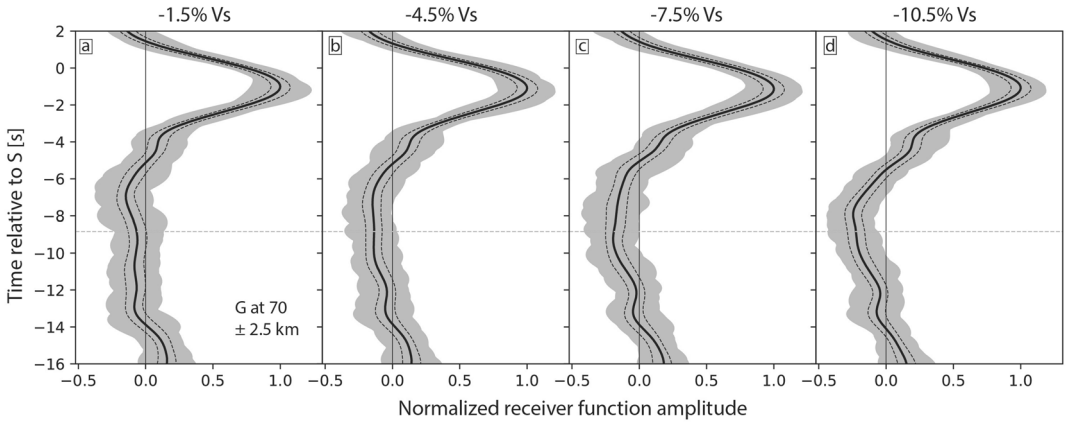


**Figure 5.** Synthetic receiver function stacks for velocity models with G present as a gradient at 70 ± 2.5 km depth, where the velocity drop across the discontinuity is varied from a 1.5% decrease in Vsv (left) up to a 10.5% decrease (right). The overall stacks are shown by solid black lines, and amplitudes are normalized to the maximum of the Moho peak in the overall stack (at approximately −1 s). Gray shading shows the range of amplitudes obtained from 300 bootstrap stacks, each with 125 samples drawn from 125 traces with replacement, and dashed black lines mark one standard deviation of amplitudes from the bootstrap stacks. The predicted arrival time for the converted phase from G is marked by the light green dashed line. The converted phase is not detectable in stacks when the magnitude of the velocity drop is small, but as the magnitude of the velocity drop increases, a negative peak emerges in the receiver function stacks at the time predicted for a converted phase arrival.

interface. Sediment velocities are based on previous studies at the NoMelt site combined with information from nearby IODP sites (Lizarralde et al., 2018; Russell et al., 2019; Shipboard Scientific Party, 2002). An Earth-flattening transformation is applied to the velocity models to account for Earth's curvature in the calculation of the synthetics. Scaled samples of noise from the data are then added, and synthetic receiver functions are calculated from the synthetic seismograms. Background noise was sampled from the OBS data in time windows prior to the direct P arrival. Since this does not include signal-generated noise, it is likely an underestimate of the true noise levels affecting the observed receiver functions. However, using noise sampled from the data helps match the frequency contents of the synthetic to the observed seismograms, and enables more robust comparisons between the two overall (e.g., Kolb & Lekić, 2014). Receiver function amplitudes are normalized for the synthetic receiver functions using the same process as the observed receiver functions: the maximum amplitude of the peak attributed to the Moho is used as the normalization factor for each velocity model. When calculated for a velocity model with a sufficiently strong shallow upper mantle discontinuity, stacks of the synthetic receiver functions show clear evidence for a converted phase (Figure 5). The converted phase is identifiable because it emerges at or very near the predicted arrival times calculated using the *TauP* toolkit (Beyreuther et al., 2010; Crotwell et al., 1999).

Synthetic receiver function stacks show that a negative peak attributable to *S*-to-*p* conversion at G is resolvable with this data set when the drop in Vsv across the G discontinuity is sufficiently strong (Figure 5). For example, for a discontinuity centered at 70 km with a total thickness of 5 km, the converted phase begins to emerge for a Vsv decrease of ∼4.5% and becomes significant at two standard deviations for a decrease of >7.5%. Whether or not G is resolvable depends on the discontinuity depth and the thickness as well as the strength: thinner and shallower features are easier to resolve for small Vsv decreases, while deeper and thicker features can only be seen in the synthetics when the associated Vsv decrease is large.

Bootstrap stacks of synthetic receiver functions indicate that the 125 traces in the data set can provide a reasonable proxy for the arrival time of the *S*-to-*p* converted phase from the model G discontinuity, but the uncertainty associated with the arrival time of the converted phase measured from a given receiver function stack is non-negligible for this quantity of data. Three hundred bootstrap stacks are calculated for each set of synthetics as described in Section 2.3, by drawing 125 random receiver functions with replacement from the set of 125 available. For a representative velocity model with G at 60 ± 2.5 km depth, the time of the negative peak corresponding to the converted phase from the model G discontinuity approaches the predicted arrival time for the converted phase as the number of traces in the stack increases (Figure 6b).

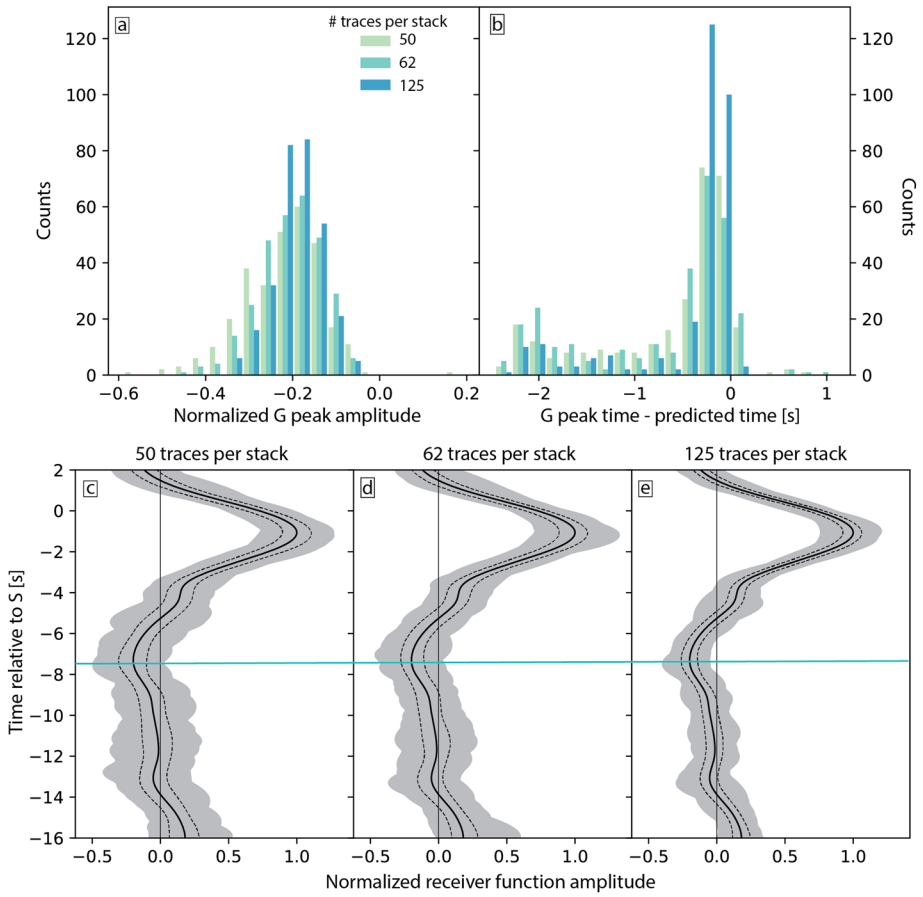


**Figure 6.** Histograms of (a) the normalized peak amplitude, and (b) the difference between the measured and predicted times for the arrival of the converted phase from the model G discontinuity, for stacks of 50-, 62-, and 125-trace samples with replacement drawn from 125 total synthetic receiver functions. The synthetics were calculated using a velocity model with G at 60 ± 2.5 km depth km and a 7.5% drop in Vsv. 300 bootstrap samples were taken for each sample size (c, d, e) Mean (solid lines) and one standard deviation (dashed lines) of bootstrap stacks for each sample size. The blue line shows the predicted arrival time of the G conversion.

The distribution of times for the negative peak is sharply peaked when the maximum number of traces is included in the stack, but with only 125 traces available there is still significant uncertainty associated with the time of the negative peak. The distribution of amplitudes for the negative peak shows that the feature is robustly negative (Figure 6a).

The uncertainty in the synthetic receiver functions comes from the noise added to the synthetic seismograms to mimic the data, and from reverberations in the sediments and water column that may interfere with converted phases. When synthetic seismograms are calculated using the simple ray-theory based code *Raysum* (Frederiksen & Bostock, 2000) instead of the reflectivity method, and realistic water and sediment multiples are not included, the resulting receiver functions are much cleaner (Figure S1).

### 2.5. Quantifying the Effects of Upper Mantle Structure on Receiver Function Stacks

We quantify the relationships between features of receiver function stacks and the depth, thickness, and strength of the model G discontinuity for a suite of 1D velocity models and corresponding synthetic receiver function stacks. We parameterize G with three quantities: the depth to the center of the discontinuity, the thickness of the velocity gradient layer comprising the discontinuity, and the percentage drop in Vsv across the discontinuity. We refer to these three parameters for G as the "G depth," "G thickness," and "G strength," respectively. The velocity models are based on a combination of local constraints from other analyses of

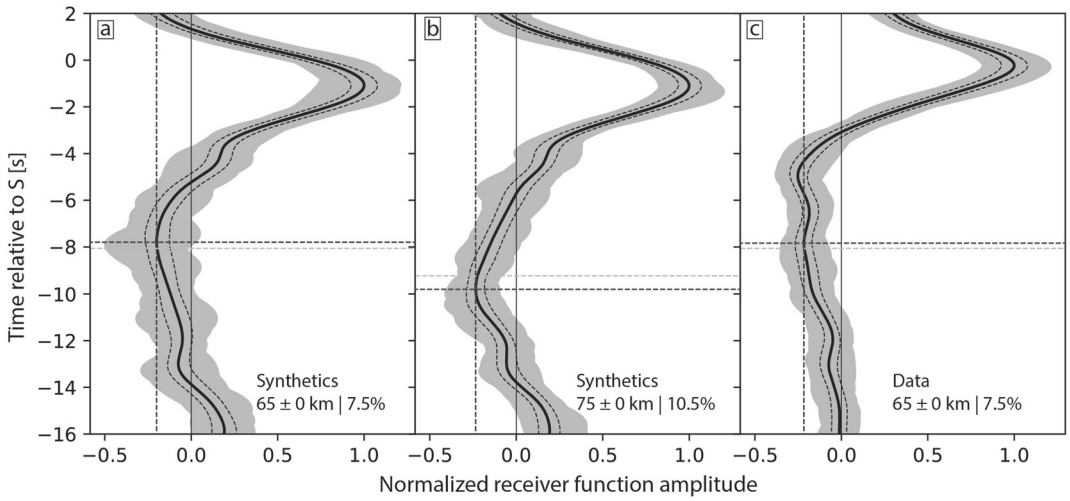


**Figure 7.** Receiver function stacks for two representative synthetic cases, and for the data with a representative moveout correction applied. The stacks are shown by the black lines, and dashed black lines show one standard deviation of amplitudes calculated from 300 bootstrap stacks and the range represented by the bootstrap stacks is shown by gray shading. Dashed dark blue lines intersect at the negative peak of each stack, marking the time and maximum amplitude of the G peak. Horizontal dashed green lines show the predicted time for the G peak based on the moveout correction model used for the stack. (a) Synthetic receiver function stack with G as a 7.5% drop in Vsv at 65 ± 0 km depth. (b) Synthetic receiver function stack with G as a 10.5% drop in Vsv at 75 ± 0 km depth. (c) Receiver function stack from NoMelt data, with moveout corrections calculated in a model where G is a 7.5% drop in Vsv at 65 ± 0 km depth.

NoMelt data (Lin et al., 2016; Lizarralde et al., 2018; Russell et al., 2019) and regional models for Pacific seismic structure (Gaherty et al., 1996). We hold the crustal structure constant, and generate a suite of 175 velocity models spanning a parameter space where the G depth is between 50 and 80 km, the G thickness is between 0 and 20 km, and the G strength is between 1.5% and 13.5% for Vsv. The velocity gradients in the mantle both above and below G vary with the strength of G. Receiver functions are sensitive to the velocity structure above a discontinuity, so varying the velocity gradient above G to accommodate the addition of the discontinuity, rather than only adjusting the gradient below G, incorporates this sensitivity into the analysis. The ranges for the depth and strength of G in the models were chosen based on previous observations of shallow upper mantle discontinuities (e.g., Collins, 2002; Gaherty et al., 1996; Kawakatsu et al., 2009; Kumar & Kawakatsu, 2011; Tan & Helmberger, 2007), and the maximum thickness of 20 km was chosen based on the limits of resolution for *S*-to-*p* receiver functions (Rychert et al., 2007).

For each of the velocity models in this parameter space, we calculate a set of synthetic seismograms and corresponding receiver functions that mimic the observations in terms of back azimuths, ranges, and moment tensors, and add noise sampled from the data to the synthetics. The seismograms are used to calculate sets of synthetic receiver functions, and each set of synthetic receiver functions is stacked using the generating velocity model for the moveout correction. The velocity model is also used to calculate a prediction for when the converted phase from the G discontinuity arrives relative to the direct *S* phase (Figures 7a and 7b).

The receiver function stack for each velocity model is analyzed to extract two main features of the stack: (1) the maximum amplitude of the G conversion peak normalized to the maximum amplitude of the positive peak due to the Moho conversion (approximately 1 s before direct *S*), and (2) the time of that maximum amplitude relative to the direct *S* arrival time. The G peak amplitude and time are picked at the local minimum of each receiver function stack within a time window around where the converted phase from G is expected to arrive (Figure 7).

The depth, thickness, and strength of G all influence both the time and the amplitude of the G peak extracted from the synthetic receiver function stacks. The strongest relationships between the parameters describing G in the velocity model and the quantities measured from the synthetic receiver function stacks are shown in Figure 8. The time of the G peak relative to the direct *S* arrival scales with G depth (Figure 8a).

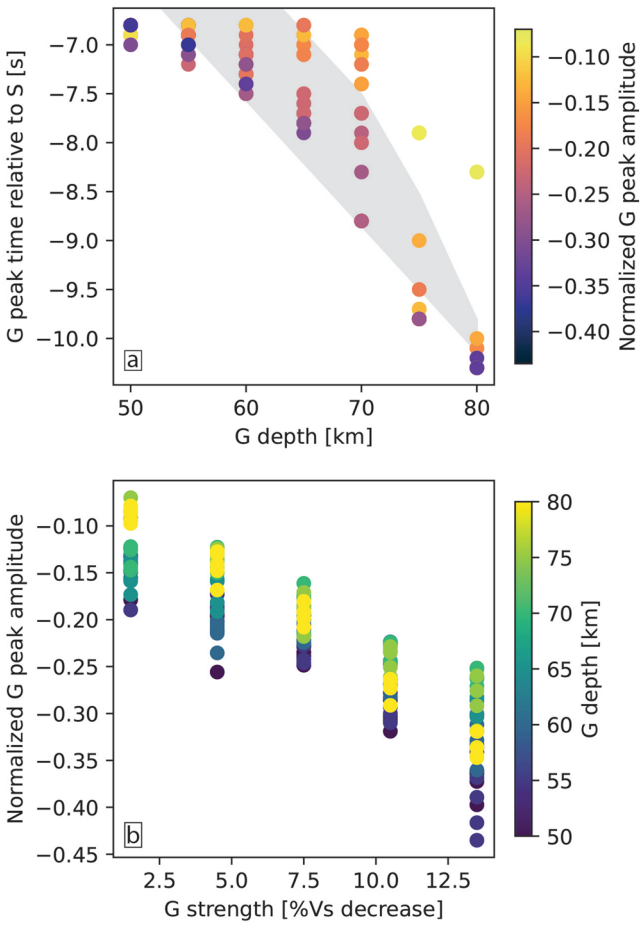


**Figure 8.** Results from synthetic receiver function stacks. (a) G peak time relative to direct *S* as a function of G depth, with points colored by normalized G peak amplitude. Note that some points overlap in the plot. Gray shading shows the range of times predicted for each G depth from raytracing. (b) Normalized G peak amplitude as a function of G strength, with points colored by G depth.

The difference between the G peak time and the direct *S* arrival is greater for cases where the G discontinuity is deeper (Figure 8a). The G peak time does not perfectly match the time predicted by raytracing for most cases. This is likely due to the filtering process, as the time of the G peak tends to be closer to the predicted time when the synthetics are calculated at higher frequencies and filtered to a wider band. The G peak amplitude decreases as G depth increases, as the converted phase amplitude in the synthetic seismograms will be smaller for conversions coming from greater depths due to geometric spreading and attenuation (Figure 8a). The amplitude of the G peak also varies strongly with G strength (Figure 8b) (Rychert et al., 2007).

Many receiver function studies seek to match the shape of receiver functions through forward-modeling (e.g., Byrnes et al., 2015; Olugboji et al., 2016); in contrast, we limit our analysis to two discrete quantities, the time and amplitude of the G peak. We do not attempt to match the shape of the G peak because our analysis is necessarily limited to constraining 1D structure at the NoMelt site and if the true structure is anisotropic or spatially heterogeneous, attempting to match the shape of the receiver functions could falsely map some of that complexity into the 1D model. Further, the suite of matched synthetics shown in Figure 8 demonstrates that the two quantities extracted from the stacks are sufficiently sensitive to the depth, thickness, and strength of G to provide useful bounds on those discontinuity parameters.

### 2.6. Estimating G Parameters from Receiver Function Stacks

The relationships between the G peak time and normalized amplitude and the depth, thickness, and strength of G for the synthetic cases described in Section 2.5 are used to constrain the unknown discontinuity structure at the NoMelt site. This is done using a gridsearch method over the parameter space of velocity models used to calculate the synthetics, where G depth, thickness, and strength are varied. We compare the time and normalized amplitude of the negative peak observed in the receiver function stack from the NoMelt data to the predictions from the synthetic receiver functions (Figure 8), and these comparisons are used to determine which velocity models in the parameter space could explain the observations.

Stacks of the observed receiver functions contain *a priori* assumptions about the discontinuity structure because a prescribed model is used to correct for moveout. We therefore repeat the process of stacking and bootstrapping the observed receiver functions for each of the velocity models in the suite used to calculate the synthetics. The choice of the moveout model is thus accounted for in estimating the G peak time and amplitude, although the contribution of the varying moveout models to the total uncertainty is small compared to the uncertainty due to noise as estimated by bootstrap stacking.

The negative peak in the observed receiver functions is robust, as demonstrated by the consistently negative amplitudes of bootstrap stacks at and around the time of the peak (e.g., Figure 7c). While the observed receiver functions show a double-peaked negative lobe that is significant at $1\sigma$ or higher from approximately −4 s to −9 s, we here define the G peak as the negative peak that is earlier with respect to direct *S* because the G discontinuity is typically defined as being a feature at depths greater than 50 km, and the earlier peak of the negative lobe would represent a shallower feature. The bootstrap stacks show that no other significant negative peaks are present in the 30 s before direct *S* (Figure S3). The normalized amplitude of the negative peak attributed to G is $-0.218 \pm 0.058$, and the time of the negative peak is $-7.95 \pm 0.65$ s. The uncertainties in the time and amplitude represent the full range of one standard deviation of values obtained from bootstrap stacks with different moveout models.

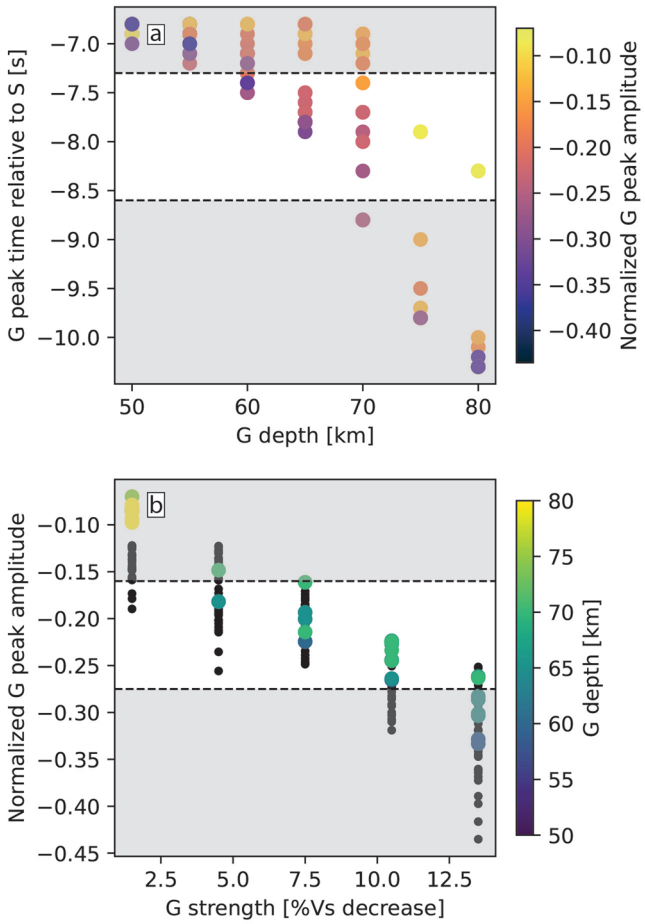


**Figure 9.** Constraining G parameters using the observed receiver functions. (a) Time of the G peak relative to direct *S* as a function of G depth with points colored by G amplitude, for synthetics. The range of G peak times observed from the data is marked by dashed black lines. (b) G amplitude as a function of G strength is plotted for synthetic stacks. Points colored by G depth correspond to synthetic stacks where the G peak time falls within the range observed for the data as shown in (a). Models where the G peak time falls outside that range are plotted as black dots. Dashed black lines mark the range of amplitudes observed for the data.

The Moho peak used to normalize the receiver function amplitudes occurs slightly closer to the direct *S* time in the observed receiver functions compared to the synthetic receiver functions. This likely results from differences between the parameters used for the sediment layer in our velocity models and the real sediments. While sediment layer velocities and thickness were set based on available constraints from the NoMelt site, sediment thickness is expected to be laterally variable and will not be perfectly represented by an average thickness. However, we note that the Moho peak times for the synthetics and the observations still overlap within the uncertainty ranges estimated via bootstrap stacking.

## 3. Results

We associate the negative peak observed at −7.95 ± 0.65 s in the stacked receiver functions with an upper mantle discontinuity that we will refer to as G (Figure 7c). The depth, thickness, and strength of this discontinuity are estimated based on comparisons between the time and amplitude of the negative peak with the same quantities derived from synthetic receiver functions (Figure 8). First, models where the G peak time from synthetics falls outside of −7.95 ± 0.65 s are excluded (Figure 9a). This constrains the G depth to 60 km or greater for the set of models tested. Second, the G peak amplitudes for the remaining viable models are compared to the observed amplitude of −0.218 ± 0.058 (Figure 9b). This comparison indicates that Vsv decreases by 4.5% or more across the discontinuity. Importantly, since we are estimating three discontinuity parameters (depth, thickness, and strength) based on two values extracted from the receiver function stacks, the problem is underdetermined and the bounds on the parameters are mutually dependent. The set of velocity models that are consistent with both the time and the amplitude of the observed G peak are shown in Figure 10 (Table S2). The mean G depth across the set of consistent models is 65 km.

The mapping between peak times and discontinuity depths for receiver functions depends on the velocity model prescribed for shallow structure above the discontinuity. We minimize the uncertainty due to shallow structure by using independent constraints specific to the NoMelt site to set our crustal velocity model (Lizarralde et al., 2018; Russell et al., 2019) (Figure 10), but some uncertainty remains due primarily to sediments. The high Vp/Vs ratio of marine sediments means that small differences in sediment thickness result in large differences in the relative arrival times of direct and converted phases. We explored the sensitivity of the constraints on G parameters to shallow structure by varying sediment thickness and Vp/Vs within ranges observed at nearby IODP drill sites (Gealy, 1971; Pälike et al, 2010a, 2010b; Shipboard Scientific Party, 2002). Our preferred sediment model based on prior NoMelt constraints has Vp/Vs of ~8 and a thickness of 165 m. For the lowest Vp/Vs (2.4) and the minimum sediment thickness we tested (100 m), the predicted arrival time for the converted phase is ~0.4 s closer to direct *S* compared to the sediment structure used in the synthetic calculations. A shift of 0.4 s in the times obtained from the synthetics would shift the range of models that could explain the observations to slightly shallower depths. For the parameter space explored here, the net effect of a higher Vp/Vs and thicker sediment layer would be to add more models to the set consistent with the observations, pushing the mean G depth of the consistent models from 65 km up to 63 km.

Variations in sediment parameters may also influence the amplitude of the Moho peak and thus the normalized receiver function amplitudes and G strength estimates. Synthetic receiver functions calculated with the range of sediment parameters described above do show variations in the amplitude of the Moho peak. Compared to models using our preferred sediment parameters based on prior constraints, other sediment

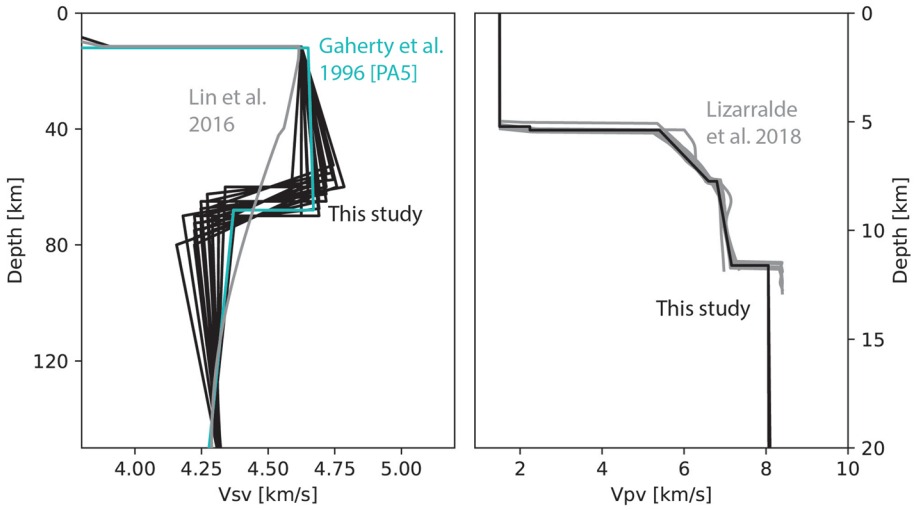


**Figure 10.** The set of velocity models consistent with the receiver functions in black, compared to the Vsv model from surface waves (gray, left), Vsv from the PA5 velocity model (blue, left), and the crustal Vp model below several individual OBS from active-source data (gray, right) (Gaherty et al., 1996; Lin et al., 2016; Lizarralde et al., 2018). 0 km depth corresponds to the sea surface. The velocity models shown in black are given in Table S2.

parameters actually shrank the range of acceptable G strengths by increasing the lower bound from 4.5%. Synthetics based on our preferred sediment model therefore provide a conservative estimate for G strength.

Interpreting the receiver functions from a single stack implicitly assumes that discontinuity structure is not laterally variable. While the small quantity of available data precludes testing this assumption by performing a spatial migration or stacking receiver functions in subsets by station, the overall character of the NoMelt site suggests that upper mantle structure is likely to be homogeneous to first order. However, we note that lateral variability in discontinuity structure is possible and is not accounted for in our analysis.

The presence of seismic anisotropy is also not explicitly treated in this analysis, although if anisotropy is present it is expected to influence the receiver functions (e.g., Bianchi et al., 2010; Levin & Park, 1997, 1998). If the G discontinuity is associated with a change in seismic anisotropy, receiver function polarity is expected to vary with source-station back azimuth. The small size of this data set precludes the analysis of stacked receiver functions binned by back azimuth, and the distribution of back-azimuths has significant gaps (Figure 1). Surface wave tomography has shown that azimuthal anisotropy varies in strength and orientation with depth (Lin et al., 2016; Russell et al., 2019), suggesting that G may be associated with a change in anisotropy, but we lack sufficient data to test whether the observed discontinuity is directly linked to a change in anisotropy. In the surface wave model of Russell et al. (2019) the sharpest variation in azimuthal anisotropy occurs between 80 and 120 km depth, deeper than the discontinuity imaged by the receiver functions.

## 4. Discussion

Receiver functions from NoMelt are consistent with the presence of a seismic discontinuity at a mean depth of 65 km. The receiver functions could be explained by models where the discontinuity thickness is anywhere from 0 to 20 km and Vsv decreases by >4.5%. The majority of the models consistent with the observations have discontinuity thicknesses of 0–10 km and strengths of 7.5%–10.5%. The depth and thickness of this discontinuity are in good agreement with studies that have used other methods to study upper mantle discontinuity structure at proximal sites (68 km, Gaherty et al., 1996; 66 km, Tan & Helmberger, 2007; 71 ± 6 km in Bin 136, Tharimena et al., 2017). Oceanic receiver function studies remain sparse, mainly because of the inherent difficulty of obtaining data from locations other than ocean islands, but several other studies have imaged discontinuities at similar depths in mature oceanic lithosphere (>40 Myr) (e.g., 76 ± 1.8 km, Kawakatsu et al., 2009; Kumar & Kawakatsu, 2011; ~70 km, Olugboji et al., 2016; 70 ± 4 km, Rychert & Shearer, 2009, 2011) and, in at least one case, in younger lithosphere (58 ± 2.93 at ~22 Myr,

Reeves et al., 2015). Analyses of velocity gradients from global tomography models also suggest that a seismic discontinuity is present throughout much of the ocean basins at a roughly constant 60–70 km depth (e.g., Lekic & Romanowicz, 2011).

The velocity gradient between the Moho and G is larger in the models consistent with the receiver functions than in the model derived from surface waves (Russell et al., 2019). This might suggest a preference for models where the G strength is smaller, resulting in a smaller gradient that comes closer to that of the surface wave model. However, both the surface wave and attenuation measurements can be fit by a model that includes a fairly strong discontinuity (Ma et al., 2020), although the surface waves cannot directly constrain such a feature.

The primary physical mechanisms proposed to explain the presence of seismic discontinuities in the upper mantle are compositional gradients due to dehydration, changes in mineral fabric, and accumulations of partial melt. Of these mechanisms, the observations from NoMelt are best explained by the presence of a dehydration gradient coupled to a change in mineral fabric.

Partial melt significantly reduces seismic velocities and has been invoked to explain observations of discontinuities both in young oceanic lithosphere (Rychert et al., 2018) and across the oceans (Kawakatsu et al., 2009; Schmerr, 2012). Although disagreements persist as to whether melt is present in the shallow upper mantle in this part of the Pacific (Debayle et al., 2020; Selway & O'Donnell, 2019), the electrical conductivity and seismic attenuation at the NoMelt site can be explained without the presence of a conductive layer indicative of partial melt accumulation (Ma et al., 2020; Matsuno & Evans, 2017; Sarafian et al., 2015). The magnitude of the velocity reduction associated with partial melt is highly dependent on the melt geometry, and models suggest that even a small melt fraction of 1% could produce up to a 7.9% reduction in Vs for melt in connected tubules and films at grain boundaries (Hammond & Humphreys, 2000; Hirschmann, 2010). However, this kind of connected melt would be highly conductive and should therefore have a signal in the magnetotelluric data. Features interpreted as melt-rich channels at the base of the lithosphere have been observed at some locations in magnetotelluric studies (e.g., Naif et al., 2013). This type of signal is absent at the NoMelt site. However, the receiver functions do not preclude the presence of crystallized melt trapped in the lithosphere due to incomplete melt extraction (Lizarralde et al., 2004).

The observed discontinuity could be explained by the presence of a dehydration boundary. The electrical structure is consistent with a 60–80 km thick resistive lid (Figure 1), indicative of a dry layer above mantle material with a higher water content (Matsuno & Evans, 2017; Sarafian et al., 2015). The mantle attenuation structure at the NoMelt site transitions from low to high attenuation at ~70 km depth, similarly consistent with the presence of a dry lid overlying a more hydrous mantle (Ma et al., 2020). Multi-phase seismic velocity models for nearby corridors across the Pacific plate that include a discontinuity parameterized as a step function also show evidence for a discontinuity around 60–70 km depth that has been interpreted as a dehydration boundary (Gaherty et al., 1996; Tan & Helmberger, 2007). These observations agree well with models that predict a dehydration boundary at ~60–70 km depth within the oceanic upper mantle due to the extraction of water during melting at mid-ocean ridges (Hirth & Kohlstedt, 1996). Models suggest that the resulting contrast in water content could generate a decrease of 5%–10% in Vs through the mechanism of elastically accommodated grain boundary sliding (EAGBS) (Karato, 2012; Olugboji et al., 2013), potentially sufficient to explain the receiver function observations. However, whether or not EAGBS is required to explain polycrystal anelasticity remains a subject of debate, and some experiments suggest that diffusionally accommodated grain boundary sliding (DAGBS) could instead provide a sub-solidus mechanism for the high-frequency peak observed in attenuation spectra (Takei, 2017; Yamauchi & Takei, 2016).

A dehydration boundary is likely to be coupled to a change in mineral fabric and seismic anisotropy, as the change in viscosity associated with dehydration is expected to influence mantle flow and fabric development beneath the young oceanic plate. To assess the potential effects of a strong gradient in water content on fabric development, we ran models of strain accumulation due to 1D channel flow (Behn et al., 2009). These models use a composite diffusion-dislocation creep rheology to parameterize the effects of temperature, grain size evolution, and water content. We investigate two cases: one with a constant water content of 1000 H/$10^6$ Si (Figure 11a), and a second with a decrease in water content from 1,000 to 50 H/$10^6$ Si imposed across a dehydration boundary between 50 and 70 km depth (Figure 11b).

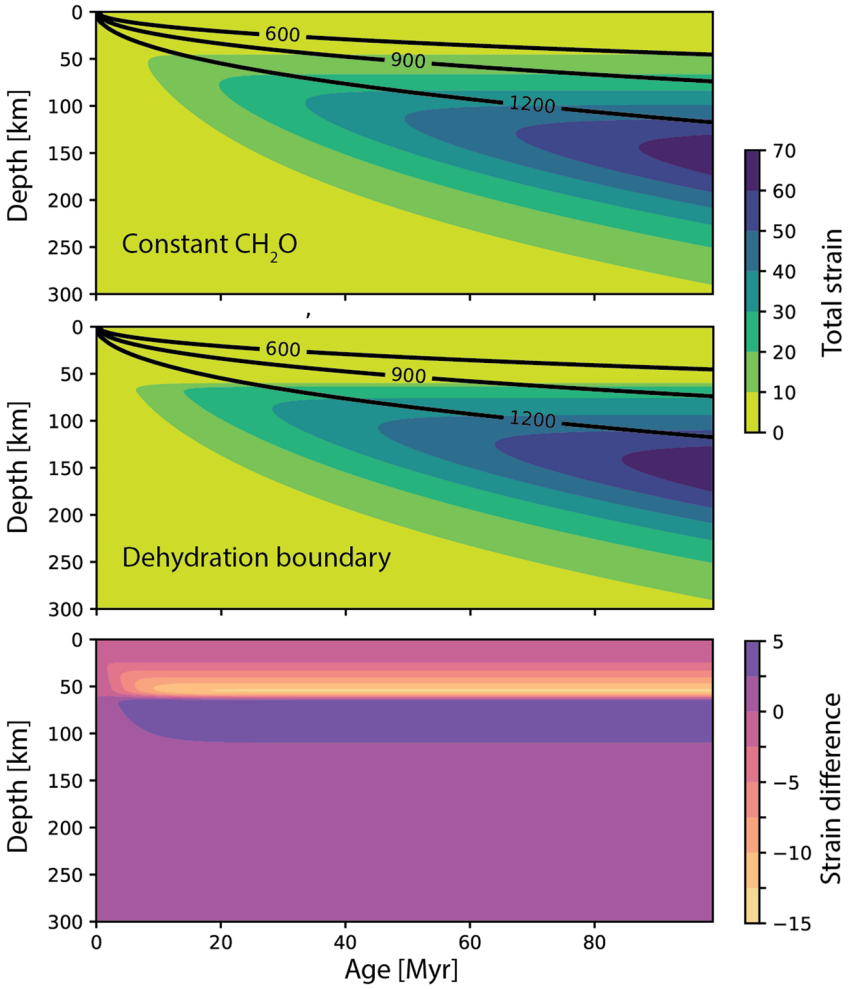


**Figure 11.** Models of accumulated strain due to one-dimensional (1D) channel flow including the effects of temperature, grain size evolution, and water content based on the model of Behn et al. (2009). The top two panels show cumulative strain as a function of depth and plate age for cases with constant water content of 1000 H/$10^6$ Si and with a smooth transition from 1,000 to 50 H/$10^6$ Si between 70 and 50 km depth, respectively. Isotherms from a half-space cooling model are shown in black. The bottom panel shows the difference in cumulative strain between the two cases.

Both models show that the locus of plate-driven shear deepens as the thermal boundary layer grows with increasing plate age. However, the presence of a dehydration boundary leads to the development of a sharper high strain gradient at the depth of the imposed dehydration boundary after ~5–10 Myr (Figure 11c). These relatively simple models are based on 1D channel flow and do not include the full corner flow patterns associated with mid-ocean ridge spreading. Nonetheless, they suggest that plate cooling causes the thermal boundary layer to thicken past the dehydration-generated strain gradient at ~30–40 Myr (Figure 11b), thereby locking this strain gradient into the lithosphere. This effective discontinuity in strain is expected to generate a corresponding change in anisotropic fabric, thus influencing the mantle velocity structure. Notably, observations of seismic discontinuities in the Pacific upper mantle show a relationship between depth and plate age out to ~40 Myr, while discontinuity depths are largely age-independent past 40 Myr (e.g., Rychert & Harmon, 2018; Tharimena et al., 2017).

The depth to an apparent rheologic contrast implied by the receiver functions, as well as other NoMelt observations, suggests that relative motion between the lithosphere and asthenosphere is accommodated across a transitional zone that is on the order of 10s of km thick. Notably, recent seismic reflection studies have found evidence for low-velocity channels at the base of the plate with thicknesses on the order of ~10 km which may represent such a transitional zone (Mehouachi & Singh, 2018; Stern et al., 2015). The

mean depth of the discontinuity imaged by receiver functions in this study is 65 km, and Vsv, azimuthal anisotropy, conductivity, and attenuation observed at the NoMelt site all undergo transitions between ~60 and 80 km depth (Lin et al., 2016; Ma et al., 2020; Russell et al., 2019; Sarafian et al., 2015). The depth resolution of the other measurements is necessarily limited, but the approximate co-occurrence of these transitions suggests some degree of connection between the changes in smooth structure and the observed discontinuity. We interpret the receiver functions as evidence for a dehydration boundary, which is expected to correspond to a rheologic contrast and localize some strain in a narrow region. Similarly, the changes in anisotropy imply a change in rheology which preserves fossil spreading-parallel fabric in the shallow mantle while allowing continued fabric evolution at greater depths (Lin et al., 2016; Russell et al., 2019). In this interpretation, both the discontinuity and the transition in anisotropy are associated with the presence of a dehydration boundary, with the discontinuity representing the velocity drop due to the compositional change and the rotation of the anisotropic fast direction resulting from subsequent strain influenced by the rheologic changes accompanying dehydration. Overall, this suggests that the effective lithosphere-asthenosphere transition is not a discrete boundary but rather a shear zone with an embedded discontinuity.

## 5. Conclusions

We have imaged a shallow upper mantle seismic discontinuity at the NoMelt site in the central Pacific. Combined constraints from the receiver functions, smooth seismic structure, and electrical structure at this site indicate that the observed discontinuity does not correspond to partial melt but can be explained by the presence of a dehydration boundary that helps to localize strain between the lithosphere and asthenosphere. We associate the observed discontinuity with the G discontinuity, a feature observed at roughly constant depths across much of the oceanic upper mantle. The receiver functions are consistent with the presence of a discontinuity at ~65 km depth with a thickness of 0–20 km and a Vsv drop of >4.5%. Comparisons to roughly co-occurring transitions in Vsv, azimuthal anisotropy, conductivity, and attenuation between ~60 and 80 km depth suggest that the discontinuity does not represent a discrete lithosphere-asthenosphere boundary, but could be associated with a broader transition zone between the rigid plate and the deforming mantle.

This study demonstrates the utility of combining different types of geophysical measurements to investigate local oceanic upper mantle structure. The context provided by local constraints on the seismic and electrical structure of the mantle enables us to better interpret the receiver function results, and the receiver functions in turn add a constraint that can be used to refine the seismic models for the NoMelt site in the future.

**Acknowledgments**
The authors thank the Captains and crews of the R/V Marcus G. Langseth and the R/V Melville, and the OBS engineers and technicians from the Scripps Institution of Oceanography and the Woods Hole Oceanographic Institution. The professionalism and expertise of these individuals were key to the success of the NoMelt experiment. The authors also thank Emily Hopper for her helpful advice on receiver functions. Three anonymous reviewers provided helpful comments and suggestions that greatly improved this manuscript. The data used in this research were recorded by instruments from the Ocean Bottom Seismograph Instrument Pool (www.obsip.org), which is funded by the National Science Foundation. This work was supported by NSF grant OCE-0928663 to D. Lizarralde, J. Collins, and R. Evans, NSF grant OCE-0927172 to G. Hirth, NSF grant OCE-0928270 to J. Gaherty, NSF grant EAR-1624109 to M. Behn, and an NSF Graduate Research Fellowship to H. Mark.

## Data Availability Statement

OBSIP data are archived at the IRIS Data Management Center (www.iris.edu). The OBS data described here are archived under network code ZA 2011–2013. The map in Figure 2 was made using the Generic Mapping Tool, GMT (Wessel et al., 2013).

## References

Barckhausen, U., Bagge, M., & Wilson, D. S. (2013). Seafloor spreading anomalies and crustal ages of the Clarion-Clipperton Zone. *Marine Geophysical Researches*, *34*(2), 79–88. https://doi.org/10.1007/s11001-013-9184-6

Becker, T. W. (2008). Azimuthal seismic anisotropy constrains net rotation of the lithosphere. *Geophysical Research Letters*, *35*(5). L5303. https://doi.org/10.1029/2007GL032928

Beghein, C., Yuan, K., Schmerr, N., & Xing, Z. (2014). Changes in seismic anisotropy shed light on the nature of the Gutenberg discontinuity. *Science*, *343*(6176), 1237–1240. https://doi.org/10.1126/science.1246724

Behn, M. D., Hirth, G., & Elsenbeck, J. R., II (2009). Implications of grain size evolution on the seismic structure of the oceanic upper mantle. *Earth and Planetary Science Letters*, *282*(1–4), 178–189. https://doi.org/10.1016/j.epsl.2009.03.014

Beyreuther, M., Barsch, R., Krischer, L., Megies, T., Behr, Y., & Wassermann, J. (2010). ObsPy: A python toolbox for seismology. *Seismological Research Letters*, *81*(3), 530–533. https://doi.org/10.1785/gssrl.81.3.530

Bianchi, I., Park, J., Piana Agostinetti, N., & Levin, V. (2010). Mapping seismic anisotropy using harmonic decomposition of receiver functions: An application to Northern Apennines, Italy. *Journal of Geophysical Research*, *115*, B12317. https://doi.org/10.1029/2009jb007061

Braun, M., Hirth, G., & Parmentier, E. M. (2000). The effects of deep damp melting on mantle flow and melt generation beneath mid-ocean ridges. *Earth and Planetary Science Letters*, *176*(3), 339–356. https://doi.org/10.1016/s0012-821x(00)00015-7

Byrnes, J. S., Hooft, E. E. E., Toomey, D. R., Villagómez, D. R., Geist, D. J., & Solomon, S. C. (2015). An upper mantle seismic discontinuity beneath the Galápagos Archipelago and its implications for studies of the lithosphere-asthenosphere boundary. *Geochemistry, Geophysics, Geosystems*, *16*(4), 1070–1088. https://doi.org/10.1002/2014gc005694

Collins, J. A. (2002). Upper mantle structure beneath the Hawaiian swell: Constraints from the ocean seismic network pilot experiment. *Geophysical Research Letters*, *29*(11). https://doi.org/10.1029/2001gl013302

Conrad, C. P., Behn, M. D., & Silver, P. G. (2007). Global mantle flow and the development of seismic anisotropy: Differences between the oceanic and continental upper mantle. *Journal of Geophysical Research*, *112*, B07317. https://doi.org/10.1029/2006jb004608

Crotwell, H. P., Owens, T. J., & Ritsema, J. (1999). The TauP toolkit: Flexible seismic travel-time and ray-path utilities. *Seismological Research Letters*, *70*(2), 7. https://doi.org/10.1785/gssrl.70.2.154

Debayle, E., Bodin, T., Durand, S., & Ricard, Y. (2020). Seismic evidence for partial melt below tectonic plates. *Nature*, *586*(7830), 555–559. https://doi.org/10.1038/s41586-020-2809-4

Dziewonski, A. M., & Anderson, D. L. (1981). Preliminary reference Earth model. *Physics of the Earth and Planetary Interiors*, *25*(4), 297–356. https://doi.org/10.1016/0031-9201(81)90046-7

Faul, U., & Jackson, I. (2005). The seismological signature of temperature and grain size variations in the upper mantle. *Earth and Planetary Science Letters*, *234*(1), 119–134. https://doi.org/10.1016/j.epsl.2005.02.008

Fischer, K. M., Ford, H. A., Abt, D. L., & Rychert, C. A. (2010). The lithosphere-asthenosphere boundary. *Annual Review of Earth and Planetary Sciences*, *38*(1), 551–575. https://doi.org/10.1146/annurev-earth-040809-152438

Frederiksen, A. W., & Bostock, M. G. (2000). Modeling teleseismic waves in dipping anisotropic structures. *Geophysical Journal International*, *141*(2), 401–412. https://doi.org/10.1046/j.1365-246x.2000.00090.x

Gaherty, J. B., Jordan, T. H., & Gee, L. S. (1996). Seismic structure of the upper mantle in a central Pacific corridor. *Journal of Geophysical Research*, *101*(B10), 22291–22309. https://doi.org/10.1029/96jb01882

Gealy, E. L. (1971). Glomar Challenger (Volume 57. https://doi.org/10.2973/dsdp.proc.7.1971Sound velocity, elastic constants, and related properties of marine sediments in the western equatorial Pacific: Leg 7

Ghosh, A., Holt, W. E., Wen, L., Haines, A. J., & Flesch, L. M. (2008). Joint modeling of lithosphere and mantle dynamics elucidating lithosphere-mantle coupling. *Geophysical Research Letters*, *35*(16). L16309. https://doi.org/10.1029/2008gl034365

Gutenberg, B. (1959). The asthenosphere low-velocity layer. *Annals of Geophysics*, *12*(4), 439–460. https://doi.org/10.4401/ag-5730

Hammond, W. C., & Humphreys, E. D. (2000). Upper mantle seismic wave velocity: Effects of realistic partial melt geometries. *Journal of Geophysical Research*, *105*(B5), 10975–10986. https://doi.org/10.1029/2000jb900041

Helffrich, G. (2006). Extended-time multitaper frequency domain cross-correlation receiver-function estimation. *Bulletin of the Seismological Society of America*, *96*(1), 344–347. https://doi.org/10.1785/0120050098

Hirano, N. (2011). Petit-spot volcanism: A new type of volcanic zone discovered near a trench. *Geochemical Journal*, *45*(2), 157–167. https://doi.org/10.2343/geochemj.1.0111

Hirschmann, M. M. (2010). Partial melt in the oceanic low velocity zone. *Physics of the Earth and Planetary Interiors*, *179*(1–2), 60–71. https://doi.org/10.1016/j.pepi.2009.12.003

Hirth, G., & Kohlstedt, D. L. (1996). Water in the oceanic upper mantle: implications for rheology, melt extraction and the evolution of the lithosphere. *Earth and Planetary Science Letters*, *144*(1–2), 93–108. https://doi.org/10.1016/0012-821x(96)00154-9

Höink, T., Jellinek, A. M., & Lenardic, A. (2011). Viscous coupling at the lithosphere-asthenosphere boundary. *Geochemistry, Geophysics, Geosystems*, *12*(10), Q0AK02. https://doi.org/10.1029/2011gc003698

Hopper, E., Ford, H. A., Fischer, K. M., Lekic, V., & Fouch, M. J. (2014). The lithosphere-asthenosphere boundary and the tectonic and magmatic history of the northwestern United States. *Earth and Planetary Science Letters*, *402*, 69–81. https://doi.org/10.1016/j.epsl.2013.12.016

Jackson, I., Gerald, J. D. F., Faul, U. H., & Tan, B. H. (2002). Grain-size-sensitive seismic wave attenuation in polycrystalline olivine. *Journal of Geophysical Research*, *107*(B12), ECV 5-1-ECV 5-16. https://doi.org/10.1029/2001jb001225

Karato, S.-I. (2012). On the origin of the asthenosphere. *Earth and Planetary Science Letters*, *321–322*, 95–103. https://doi.org/10.1016/j.epsl.2012.01.001

Kawakatsu, H., Kumar, P., Takei, Y., Shinohara, M., Kanazawa, T., Araki, E., & Suyehiro, K. (2009). Seismic evidence for sharp lithosphere-asthenosphere boundaries of oceanic plates. *Science*, *324*(5926), 499–502. https://doi.org/10.1126/science.1169499

Kennett, B. L. N., Engdahl, E. R., & Buland, R. (1995). Constraints on seismic velocities in the Earth from traveltimes. *Geophysical Journal International*, *122*(1), 108–124. https://doi.org/10.1111/j.1365-246x.1995.tb03540.x

Kennett, B. L. N., & Kerry, N. J. (1979). Seismic waves in a stratified half space. *Geophysical Journal International*, *57*(3), 557–583. https://doi.org/10.1111/j.1365-246x.1979.tb06779.x

Kolb, J. M., & Lekić, V. (2014). Receiver function deconvolution using transdimensional hierarchical Bayesian inference. *Geophysical Journal International*, *197*(3), 1719–1735. https://doi.org/10.1093/gji/ggu079

Kumar, P., & Kawakatsu, H. (2011). Imaging the seismic lithosphere-asthenosphere boundary of the oceanic plate. *Geochemistry, Geophysics, Geosystems*, *12*(1). https://doi.org/10.1029/2010gc003358

Kumar, P., Kind, R., Hanka, W., Wylegalla, K., Reigber, C., Yuan, X., et al. (2005). The lithosphere-asthenosphere boundary in the North-West Atlantic region. *Earth and Planetary Science Letters*, *236*(1–2), 249–257. https://doi.org/10.1016/j.epsl.2005.05.029

Lekić, V., & Romanowicz, B. (2011). Tectonic regionalization without a priori information: A cluster analysis of upper mantle tomography. *Earth and Planetary Science Letters*, *308*(1–2), 151–160. https://doi.org/10.1016/j.epsl.2011.05.050

Lenardic, A., Richards, M. A., & Busse, F. H. (2006). Depth-dependent rheology and the horizontal length scale of mantle convection. *Journal of Geophysical Research*, *111*, B07404. https://doi.org/10.1029/2005jb003639

Levin, V., & Park, J. (1997). P-SH conversions in a flat-layered medium with anisotropy of arbitrary orientation. *Geophysical Journal International*, *131*(2), 253–266. https://doi.org/10.1111/j.1365-246x.1997.tb01220.x

Levin, V., & Park, J. (1998). P-SH conversions in layered media with hexagonally symmetric anisotropy: A cookbook. *Pure and Applied Geophysics*, *151*, 669–697. https://doi.org/10.1007/s000240050136

Lin, P.-Y. P., Gaherty, J. B., Jin, G., Collins, J. A., Lizarralde, D., Evans, R. L., & Hirth, G. (2016). High-resolution seismic constraints on flow dynamics in the oceanic asthenosphere. *Nature*, *535*(7613), 538–541. https://doi.org/10.1038/nature18012

Lizarralde, D., Gaherty, J. B., Collins, J. A., Hirth, G., & Evans, R. L. (2018). A Lithospheric-Mantle Phase Boundary at 30 Km Depth beneath the Northeast Pacific NoMelt Site Volume 23. AGU Fall Meeting Abstracts. Retrieved from http://adsabs.harvard.edu/abs/2018AGUFM.T23E0427L

Lizarralde, D., Gaherty, J. B., Collins, J. A., Hirth, G., & Kim, S. D. (2004). Spreading-rate dependence of melt extraction at mid-ocean ridges from mantle seismic refraction data. *Nature*, *432*(7018), 744–747. https://doi.org/10.1038/nature03140

Maggi, A., Debayle, E., Priestley, K., & Barruol, G. (2006). Multimode surface waveform tomography of the Pacific Ocean: a closer look at the lithospheric cooling signature. *Geophysical Journal International*, *166*(3), 1384–1397. https://doi.org/10.1111/j.1365-246x.2006.03037.x

Mark, H. F., Lizarralde, D., Collins, J. A., Miller, N. C., Hirth, G., Gaherty, J. B., & Evans, R. L. (2019). Azimuthal seismic anisotropy of 70-Ma Pacific-plate upper mantle. *Journal of Geophysical Research: Solid Earth*. https://doi.org/10.1029/2018JB016451

Matsuno, T., & Evans, R L. (2017). Constraints on lithospheric mantle and crustal anisotropy in the NoMelt area from an analysis of long-period seafloor magnetotelluric data. *Earth Planets and Space*, *69*(1), 138. https://doi.org/10.1186/s40623-017-0724-1

Ma, Z., Dalton, C. A., Russell, J. B., Gaherty, J. B., Hirth, G., & Forsyth, D. W. (2020). Shear attenuation and anelastic mechanisms in the central Pacific upper mantle. *Earth and Planetary Science Letters*, *536*, 116148. https://doi.org/10.1016/j.epsl.2020.116148

Mehouachi, F., & Singh, S. C. (2018). Water-rich sublithospheric melt channel in the equatorial Atlantic Ocean. *Nature Geoscience*, *11*(1), 65–69. https://doi.org/10.1038/s41561-017-0034-z

Montagner, J.-P., & Nataf, H.-C. (1986). A simple method for inverting the azimuthal anisotropy of surface waves. *Journal of Geophysical Research*, *91*(B1), 511–520. https://doi.org/10.1029/jb091ib01p00511

Naif, S., Key, K., Constable, S., & Evans, R. L. (2013). Melt-rich channel observed at the lithosphere-asthenosphere boundary. *Nature*, *495*(7441), 356–359. https://doi.org/10.1038/nature11939

Olugboji, T. M., Karato, S., & Park, J. (2013). Structures of the oceanic lithosphere-asthenosphere boundary: Mineral-physics modeling and seismological signatures. *Geochemistry, Geophysics, Geosystems*, *14*(4), 880–901. https://doi.org/10.1002/ggge.20086

Olugboji, T. M., Park, J., Karato, S.-i., & Shinohara, M. (2016). Nature of the seismic lithosphere-asthenosphere boundary within normal oceanic mantle from high-resolution receiver functions. *Geochemistry, Geophysics, Geosystems*, *17*(4), 1265–1282. https://doi.org/10.1002/2015gc006214

Pälike, H., Lyle, M., Nishi, H., Raffi, I., Gamage, K., & Klaus, A. (2010a). Expedition 320/321 scientists Volume *320/321*. Integrated Ocean Drilling Program. Site U1331. https://doi.org/10.2204/iodp.proc.320321.2010

Pälike, H., Lyle, M., Nishi, H., Raffi, I., Gamage, K., & Klaus, A. (2010b). Expedition 320/321 scientists (Volume *320/321*. Integrated Ocean Drilling Program. Site U1332. https://doi.org/10.2204/iodp.proc.320321.2010

Park, J., & Levin, V. (2000). Receiver functions from multiple-taper spectral correlation estimates. *Bulletin of the Seismological Society of America*, *90*(6), 1507–1520. https://doi.org/10.1785/0119990122

Park, J., Lindberg, C. R., & Vernon, F. L. (1987). Multitaper spectral analysis of high-frequency seismograms. *Journal of Geophysical Research*, *92*(B12), 12675–12684. https://doi.org/10.1029/jb092ib12p12675

Phipps Morgan, J. (1997). The generation of a compositional lithosphere by mid-ocean ridge melting and its effect on subsequent off-axis hotspot upwelling and melting. *Earth and Planetary Science Letters*, *146*(1–2), 213–232. https://doi.org/10.1016/s0012-821x(96)00207-5

Reeves, Z., Lekić, V., Schmerr, N., Kohler, M., & Weeraratne, D. (2015). Lithospheric structure across the California Continental Borderland from receiver functions. *Geochemistry, Geophysics, Geosystems*, *16*(1), 246–266. https://doi.org/10.1002/2014gc005617

Revenaugh, J., & Jordan, T. H. (1991). Mantle layering fromScSreverberations: 3. The upper mantle. *Journal of Geophysical Research*, *96*(B12), 19781–19810. https://doi.org/10.1029/91jb01487

Richards, M. A., & Lenardic, A. (2018). The Cathles Parameter (Ct): A geodynamic definition of the asthenosphere and implications for the nature of plate tectonics. *Geochemistry, Geophysics, Geosystems*. https://doi.org/10.1029/2018gc007664

Richards, M. A., Yang, W.-S., Baumgardner, J. R., & Bunge, H.-P. (2001). Role of a low-viscosity zone in stabilizing plate tectonics: Implications for comparative terrestrial planetology. *Geochemistry, Geophysics, Geosystems*, *2*(8). 2000GC000115. https://doi.org/10.1029/2000gc000115

Russell, J. B., Gaherty, J. B., Lin, P.-Y. P., Lizarralde, D., Collins, J. A., Hirth, G., & Evans, R. L. (2019). High-resolution constraints on pacific upper mantle petrofabric inferred from surface-wave anisotropy. *Journal of Geophysical Research: Solid Earth*. https://doi.org/10.1029/2018JB016598

Rychert, C. A., & Harmon, N. (2018). Predictions and observations for the oceanic lithosphere from S -to- P receiver functions and SS precursors. *Geophysical Research Letters*, *45*(11), 5398–5406. https://doi.org/10.1029/2018gl077675

Rychert, C. A., Harmon, N., & Tharimena, S. (2018). Scattered wave imaging of the oceanic plate in Cascadia. *Science Advances*, *4*(2), eaao1908. https://doi.org/10.1126/sciadv.aao1908

Rychert, C. A., Rondenay, S., & Fischer, K. M. (2007). P-to-S and S-to-P imaging of a sharp lithosphere-asthenosphere boundary beneath eastern North America. *Journal of Geophysical Research*, *112*(B8). https://doi.org/10.1029/2006jb004619

Rychert, C. A., & Shearer, P. M. (2009). A global view of the lithosphere-asthenosphere boundary. *Science*, *324*(5926), 495–498. https://doi.org/10.1126/science.1169754

Rychert, C. A., & Shearer, P. M. (2011). Imaging the lithosphere-asthenosphere boundary beneath the Pacific using SS waveform modeling. *Journal of Geophysical Research*, *116*(B7). https://doi.org/10.1029/2010jb008070

Sarafian, E., Evans, R. L., Collins, J. A., Elsenbeck, J., Gaetani, G. A., Gaherty, J. B., et al. (2015). The electrical structure of the central Pacific upper mantle constrained by the NoMelt experiment. *Geochemistry, Geophysics, Geosystems*, *16*(4), 1115–1132. https://doi.org/10.1002/2014gc005709

Savage, M. K. (1999). Seismic anisotropy and mantle deformation: What have we learned from shear wave splitting?. *Reviews of Geophysics*, *37*(1), 65–106. https://doi.org/10.1029/98rg02075

Schmerr, N. (2012). The Gutenberg discontinuity: Melt at the lithosphere-asthenosphere boundary. *science*, *335*(6075), 1480–1483. https://doi.org/10.1126/science.1215433

Selway, K., & O'Donnell, J. P. (2019). A small, unextractable melt fraction as the cause for the low velocity zone. *Earth and Planetary Science Letters*, *517*, 117–124. https://doi.org/10.1016/j.epsl.2019.04.012

Shibutani, T., Ueno, T., & Hirahara, K. (2008). Improvement in the extended-time multitaper receiver function estimation technique. *Bulletin of the Seismological Society of America*, *98*(2), 812–816. https://doi.org/10.1785/0120070226

Shipboard Scientific Party. (2002). Leg 199 preliminary report. *ODP Preliminary Report*, *99*, 105. https://doi.org/10.2973/odp.proc.ir.199.101.2002

Solomon, S. C., & Sleep, N. H. (1974). Some simple physical models for absolute plate motions. *Journal of Geophysical Research*, *79*(17), 2557–2567. https://doi.org/10.1029/jb079i017p02557

Stern, T. A., Henrys, S. A., Okaya, D., Louie, J. N., Savage, M. K., Lamb, S., et al. (2015). A seismic reflection image for the base of a tectonic plate. *Nature*, *518*(7537), 85–88. https://doi.org/10.1038/nature14146

Stixrude, L., & Lithgow-Bertelloni, C. (2005). Mineralogy and elasticity of the oceanic upper mantle: Origin of the low-velocity zone. *Journal of Geophysical Research*, *110*, B03204. https://doi.org/10.1029/2004jb002965

Swindell, W. H., & Snell, N. S. (1977). Station processor automatic signal detection system, phase I: Final report, station processor software development. *Texas Instruments Final Report No. ALEX (01)-FR-*, *77*, 1

Takei, Y. (2017). Effects of partial melting on seismic velocity and attenuation: A new insight from experiments. *Annual Review of Earth and Planetary Sciences*, *45*(1), 447–470. https://doi.org/10.1146/annurev-earth-063016-015820

Tan, Y., & Helmberger, D. V. (2007). Trans-Pacific upper mantle shear velocity structure. *Journal of Geophysical Research*, *112*, B08301. https://doi.org/10.1029/2006jb004853

Tharimena, S., Rychert, C., Harmon, N., & White, P. (2017). Imaging Pacific lithosphere seismic discontinuities-Insights from SS precursor modeling. *Journal of Geophysical Research: Solid Earth*. https://doi.org/10.1002/2016jb013526

Wessel, P., Smith, W. H. F., Scharroo, R., Luis, J., & Wobbe, F. (2013). Generic mapping tools: Improved version released. *Eos Transactions American Geophysical Union*, *94*(45), 409–410. https://doi.org/10.1002/2013eo450001

Wilson, J. T. (1965). Evidence from ocean islands suggesting movement in the Earth. *Philosophical Transactions of the Royal Society of London - Series A: Mathematical and Physical Sciences*, *258*(1088), 145–167. https://doi.org/10.1098/rsta.1965.0029

Withers, M., Aster, R., Young, C., Beiriger, J., Harris, M., Moore, S., & Trujillo, J. (1998). A Comparison of Select Trigger Algorithms for Automated Global Seismic Phase and Event Detection. *Bulletin of the Seismological Society of America*, *88*(1), 95–106.

Yamauchi, H., & Takei, Y. (2016). Polycrystal anelasticity at near-solidus temperatures. *Journal of Geophysical Resarch Solid Earth*, *121*(11), 7790–7820. https://doi.org/10.1002/2016jb013316

Yang, J., & Faccenda, M. (2020). Intraplate volcanism originating from upwelling hydrous mantle transition zone. *Nature*, *579*(7797), 88–91. https://doi.org/10.1038/s41586-020-2045-y

Yuan, X., Kind, R., Li, X., & Wang, R. (2006). TheSreceiver functions: Synthetics and data example. *Geophysical Journal International*, *165*(2), 555–564. https://doi.org/10.1111/j.1365-246x.2006.02885.x